Variable Viscosity Jets: Entrainment and Mixing Process

Léa Voivenel[1,*], **Emilien Varea**[1], **Luminita Danaila**[1], **Bruno Renou**[1], **Michel Cazalens**[2]

[1]CORIA UMR 6614, University of Rouen, St Etienne du Rouvray, France
[2]SAFRAN Research and Technologies Centre, Magny-les-Hameaux, France
[*]corresponding author: voivenel@coria.fr

Abstract Turbulent jets have received considerable attention during the last decades. However, to our knowledge, one configuration has not received much consideration. The latter concerns the variable-viscosity jet, wherein a turbulent jet of lower viscosity issues into a density-matched host fluid of higher viscosity. In this study, we carry out a comparison between Constant Viscosity Flows (CVF) and Variable Viscosity Flows (VVF), in a round jet, on the basis of the same initial jet momentum and the same initial Reynolds number. A propane jet issues into a N_2 (slight) coflow, for which the kinematic viscosity ratio is $R_\nu \equiv \nu_{N_2}/\nu_{propane} = 3.5$. The Reynolds number of the jet (based on the diameter, the initial velocity and the propane viscosity), is of 8000. The direct interactions between the velocity and the scalar fields reflect the need to perform simultaneous measurements of these two physical quantities. The stereo Particle Image Velocimetry (stereo-PIV) and the Planar Induced Fluorescence (PLIF) have been chosen for the velocity and the concentration measurements respectively. These diagnostics are detailed and the use of an original tracer for the PLIF measurements is notably brought forward. Experimental results are discussed, for both velocity and scalar fields, in the axial plane of the turbulent axisymmetric jet. It is shown that the presence of a strong viscosity discontinuity across the jet edge results in an increase of the scalar spread rate and of the turbulent fluctuations.
Keywords: variable-viscosity, turbulence, mixing

1 Introduction

The theory of Kolmogorov premises that at infinitely large Reynolds numbers, the statistical properties of the small scales should be determined universally by ν and $\overline{\varepsilon}$ (the kinematic viscosity and the mean energy dissipation rate). Implicit to this theory is that viscosity, considered as one independent parameter of the flow, is a 'small scale' quantity and thus should not affect large scale mixing. This is one possible explanation for why most of the studies focus on homogeneous fluids (same density and viscosity), or on variable-density flows ([1], [2]). Nonetheless, many flows deal with real fluids, for which both density and viscosity fluctuate in space and time.

One of the first studies devoted to effects of viscosity was that of [3]. In order to determine the composition of a magmatic layer, they studied the injection of a fluid in a more viscous one (whose kinematic viscosities are respectively ν_l and ν_h, indices 'l' and 'h' stand for 'low' and 'high' respectively), for several ratios $R_\nu = \frac{\nu_h}{\nu_l}$ spread from 1 to 400. Reference [3] observed a very different behaviour for the two borderline-cases. Indeed, mixing does not occur at all for the $R_\nu = 400$ case. This phenomenon is due to a competition between the destabilizing inertial forces and the stabilizing viscous ones at the interface. Thus, this study highlights that the large scale mixing is in fact, greatly viscosity-dependant and that Variable-Viscosity-Flow (hereafter referred to as VVF) should be carefully studied. Indeed, this kind of flow is frequently encountered in industrial applications. To cite one example, combustion processes involve fluids with different physical and chemical properties (*e.g.* fuel and oxidizer).

Numerous questions, however, remain without clear answer. Some of them are fundamental, such as those dealing with the rate of entrainment and the associated phenomenology, or the exact expression of the mean energy dissipation rate ([4], [5]) which appears to be of great importance for flame stabilization and quenching. Hence, it is necessary to perform some qualitative experiments in more traditional aerodynamic configurations (gaseous flow and relatively high Reynolds number).

The present study aims at furthering our understanding of variable-viscosity flows. The roadmap of the paper is as follows. The section 2 details the experimental facility. Then, in Sec. 3, the optical diagnostics are presented, especially the use of a new tracer for the concentration measurements. The fourth and fifth section aim at developing results on the dynamic and scalar fields in VVF versus CVF, based on the same momentum and Reynolds number respectively. The last part is dedicated to conclusions.

2 Experimental-Setup

The effects of viscosity variations are quantified by comparing the following cases:
-Constant-Viscosity Flow (CVF), which is the baseline case. A nitrogen jet issues in a coflow of nitrogen. The viscosity ratio of the two fluids is $R_v = 1$.
-Variable-Viscosity Flow (VVF). A propane jet issues in a coflow of nitrogen. The latter is 3.5 times more viscous than the propane, so that $R_v = 3.5$. The density ratio is very nearly equal to 1. The comparison between the two cases is based on the *same initial condition*, i.e. the same initial jet momentum, therefore the same injection velocity $U_{inj} = 1.45$ m/s. To remove any ambiguity regarding the role of the Reynolds number , the comparison between CVF and VVF at the same initial Reynolds number will be done in Section 5. The flow facility is a round jet of diameter $D = 30$ mm surrounded by a (slight) coflow. Jet and coflow are enclosed in order to get well defined boundary conditions allowing future accurate numerical simulations (Fig.1). The coflow diameter, $D_{cof} = 800$ mm, is sufficiently large to restrain the wall influence on the main jet while isolating it from the exterior environment.

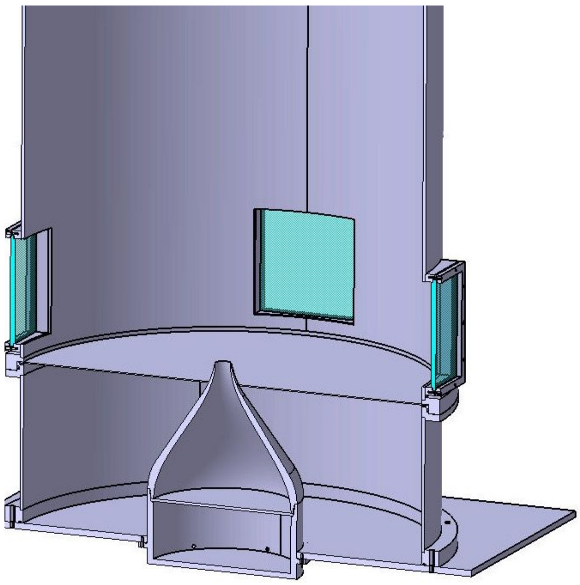

Fig. 1 Sketch of the experimental facility. Nozzle, confinement and optical accesses.

The main jet issues from a contraction designed to ensure a 'top-hat' velocity profile at the nozzle exit. To achieve this objective, the two key parameters to be chosen are:
– the contraction ratio $C_R = \frac{D_{\mathrm{in}}^2}{D_{\mathrm{out}}^2}$, with D_{in} initial diameter of the contraction and D_{out} the diameter at the contraction exit,
–the length on in-diameter ratio $\frac{L}{D_{\mathrm{out}}}$, with L the length of the contraction.
We have chosen to use the same values as [6] *i.e.* $C_R = 87$ and $\frac{L}{D_{\mathrm{in}}} \approx 1$. These parameters have then been used in the laws given by [7] to design contraction walls. The velocity profiles immediately at the nozzle exit, obtained by Hot Wire Anemometry (HWA), are consistent with those obtained by [6], Fig. 2. The initial turbulence intensity is as low as 1%, thus ensuring that the measured turbulent fluctuations do not find their origins in the injection.
The flow-rate is ensured by a Bronkhorst Coriolis Mass Flow Controller (model SNB13201070A/s) for the main jet and Bronkhorst Thermal Mass Flow Controller (model SNM4209650B) for the coflow. Both mass flow controlers have been calibrated or checked thanks to an in-house calibration bench.

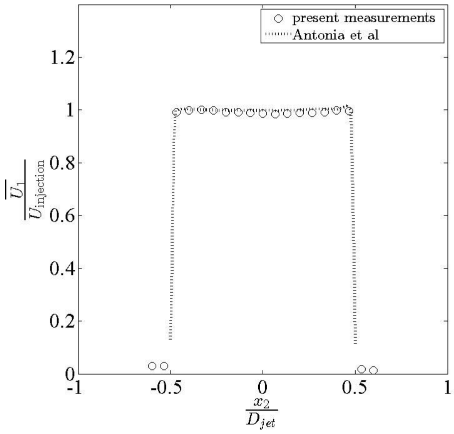

Fig. 2 Comparison of the velocity profile at the nozzle exit obtained in the current study and in [6]'s.

3 Optical Diagnostics

Velocity Measurements

Velocity field measurements were performed by stereo-Particle Image Velocimetry (stereo-PIV). The stero-PIV technique was been chosen since as far as active scalar is concerned, the round jet will lose its instantaneous axisymmetric behavior. Therefore measuring the third component of the velocity fieldis of major importance. The laser beam was issued from a Quantel Ultra Twin laser, at 532 nm. A parallel laser sheet, passing through the jet center, is obtained using a cylindrical lens with a -40 mm focal followed by a 500 mm focal spherical lens (Fig. 3). Seeding is done using Di-Ethyl-Hexyl-Sebacat (DEHS) particles whose size repartition is more homogeneous than that of vegetale oil (size order of magnitude around $1\mu m$). Two Imager ProX cameras (LaVision), coupled with two visible Nikkor 105 mm focal length and f/2.8 lens, are placed on either side of the laser sheet at a 45° angle. Each camera recorded particle images which were independently post-treated with the algorithm 'Adaptative PIV', provided by the Dantec software *Dynamic Studio* (3.4 release). Then, thanks to a previously performed calibration, the n^{th} 2D field from camera #1 is combined with the corresponding field from the camera #2, creating a single 2 dimensions-3 components (2D-3C) velocity field.

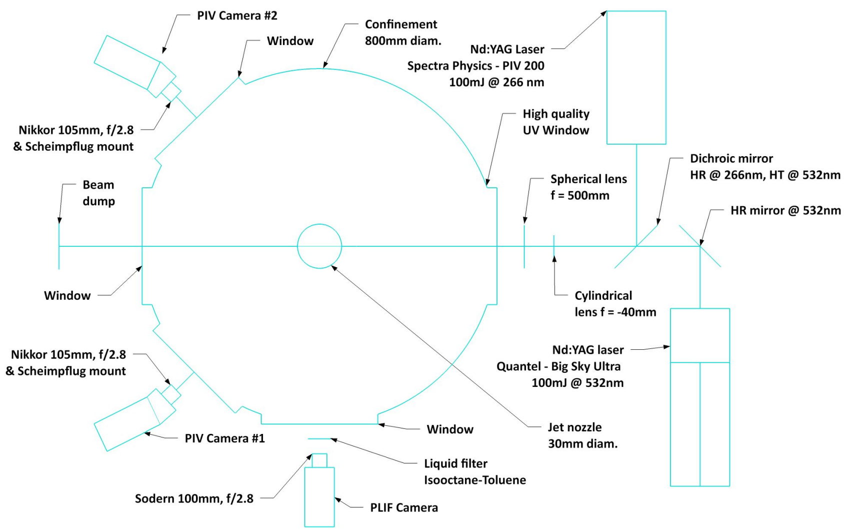

Fig. 3 Schematic diagram of the jet experiment.

Concentration Measurements

Whilst the velocity field measurements are standard, the main experimental novelty of this paper rests upon the concentration measurements. Usually, acetone molecules are used as tracer to perform Planar Laser Induced

Fluorescence (PLIF) measurements. However, in order to obtain a sufficient signal-to-noise ratio level, an important amount of tracer has to be used, leading to a modification of the seeded fluid properties. The viscosity effect being our focus, acetone is not an accurate choice in our case. Thus, we looked for an alternative molecule allowing a better signal to noise ratio while conserving the studied fluid properties. In addition to the previously discussed restrictions, the tracer must satisfy several other criteria:

- absorption wavelength has to be compatible with highly energetic laser at our disposal ($\lambda = 266$ nm)
- fluorescence spectrum must be shifted from the excitation wavelength
- evaporation properties must allow mixing with a gas
- safe for user and environment.

Therefore, several potential candidate are listed in Table 1.

Table 1 Comparative table of potential tracer properties.

Molecule	$\lambda_{\text{absorption}}$ (nm)	$\lambda_{\text{emission}}$ (nm)	$T_{boiling}$ (°C)	QR	Comment	Source
Acetone	250-320	350-550	56	0.2%	Low SNR	[8]
Acetaldheyde	250-340	350-480	21	0.1%	Carcinogenic	[8]
3-pentanone	220-320	350-350	102	1.3*acetone's	Limited toxicit	[9]
Naphtalene	266 possible	300-400	218	23%	Solid at ambiant T	[10]
Toluene	220-290	270-370	110	17% (266 Tamb)	Harmful	[9]
Anisole	240-280	270-350	154	29%	O_2 quenching	[11]

For safety reasons, our jet issues in nitrogen and not in air. Therefore, the strong quenching of anisole with O_2 is not an issue in our case. Thus, we have chosen to use anisole as a tracer for our PLIF measurements.
To validate this technique, the linearity of the PLIF signal with the laser energy and the tracer concentration was tested. An other critical point is the proximity of the anisole absorption and emission band. To eliminate the Mie signal at 266 nm coming from the DEHS particles as well as the stray light due to reflection at 266 nm, we use a liquid filter composed of isooctane (spectroscopically neutral) and toluene as suggested in [10]. Indeed, the toluene, absorbs predominantly at 266 nm and dimly from 270 nm, which is the begining of the anisole fluorescence signal (see [11]).

The tracer particles are excited using a Nd:YAG laser (Spectra Physics) with a fourth-harmonic generating crystal that produces a Q-switched laser output in the UV (λ=266 nm, 100 mJ). A dichroic mirror is used to optically combine the PIV laser beam with LIF laser beam. The fluorescence signal is collected by an intensified CCD (ICCD) camera coupled to a UV Cerco 100 mm, f/2.8 lens. The ICCD camera is a Roper Scientific PIMAX 4 (16 bits) manufactured by Princeton Instruments with a pixel format of 1024x1024 pixels^2. The exposure time is set to 500 ns which corresponds to a compromise between fluorescence signal collection and the noise level increase.
Usually to normalise PLIF images, the technique consists in *i*) correcting from laser energy distribution (mean laser sheet image), and *ii*) correcting from shot-to-shot variations using a known concentration zone within the image. To minimize the post processing noise, the method requires a good spatial homogeneity of the laser sheet. We have paid particular attention to this requirement, by selecting only a part of the incident beam before forming the laser sheet. Thus, the mean profile of the signal intensity is as close as possible to a 'top-hat' profile (Fig 4, right).
While this technique works very well in the CVF case, the presence of additional streaks in PLIF images in the Propane / N_2 case prevents its use in VVF (Fig. 4, left). These strikes comes from the slight gradient change in the mixture which modifies the refractive index [12]. Indeed, the mean laser sheet is obtained by imaging an homogeneous mixture of N_2 seeded with anisole, in which the streaks are absent (density match). The position of these streaks varies shot-to-shot, depending on the flow structures. The solution to normalise our instantaneous images should then to acquire simultaneously the information on the shot-to-shot laser sheet distribution. The difficulty in setting up another camera to acquire the instantaneous laser profile (generally imaged on a screen) is obvious. In the present configuration we can use the jet potential core since it is present

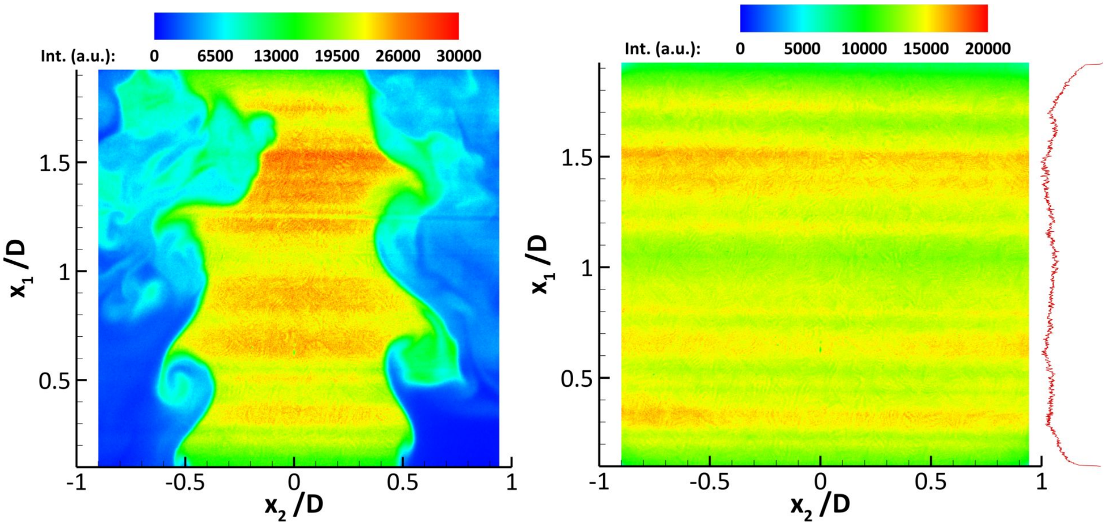

Fig. 4 Instantaneous PLIF image in VVF (left side) and mean laser sheet image (right side).

on the full height of our field of view. Thus, we obtain a shot-to-shot laser sheet profile by averaging the signal obtained at the potential core location. The normalisation is more efficient and corrects the laser sheet shot-to-shot variation, Fig. 5.

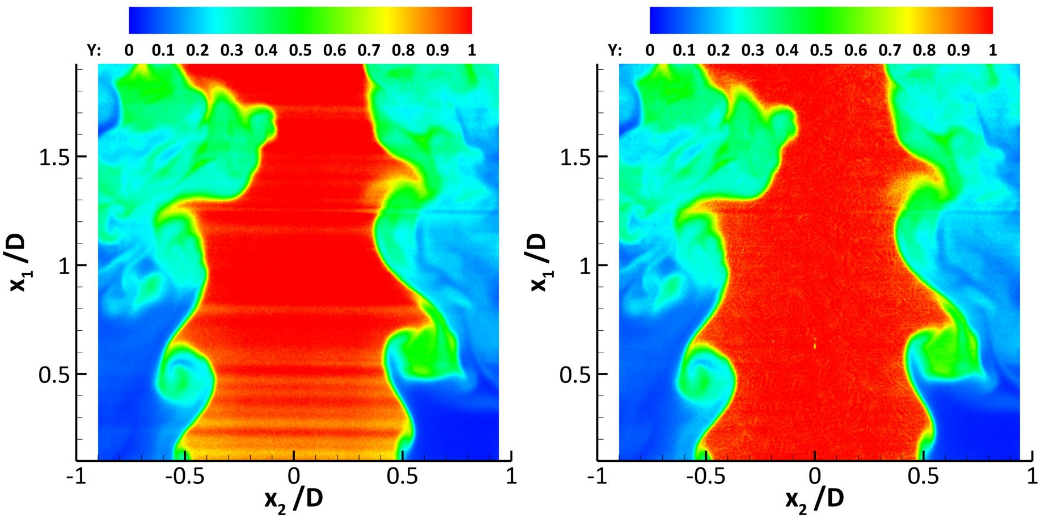

Fig. 5 Instantaneous PLIF image normalized by the mean laser sheet, left, and by a simultaneous laser sheet profile, right.

In the following sections, CVF and VVF will be compared on the basis of same jet momentum (Sec. 4) and same Re (Sec. 5), respectively.

4 Comparison of CVF and VVF based on the same initial jet momentum

Figure 6 illustrates instantaneous images of the scalar distribution. Here Y is the propane concentration – the mixture fraction– normalized such as $Y = 1$ in the propane core jet and $Y = 0$ in the N_2 coflow. A careful analysis of the scalar mixing provides a qualitative way to compare the two flows. Whilst the constant-viscosity flow exhibits classical Kelvin-Helmholtz vortices, Fig. 6, left, the variable-viscosity flow, Fig. 6, right, only includes a hint of the large-scale, lateral engulfment of the ambient fluid, living together with mixing at scales distributed over a much wider range.

Planar distributions of the mean and RMS (root mean squared) of the scalar are represented in Fig. 7, for the very near field of the flow, spanning between 0 and 2 jet diameters. Several observations may be done.

First, the CVF potential core, Fig. 7, image left-half-side, is wider than that of the VVF, Fig. 7, image right-

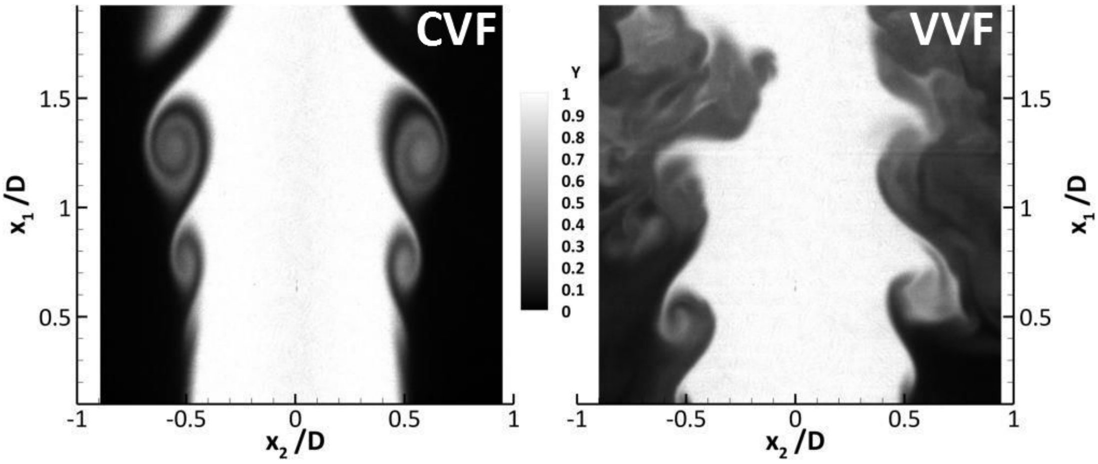

Fig. 6 Instantaneous images of mixing in N_2/N_2 jet, left, and Propane/N_2 jet, right.

half-side, which suggests a better mixing for the latter. This statement is supported by the presence of propane in the full field of view for VVF. This is in contrast with the N_2/N_2 jet, where the core jet fluid (seeded N_2) is completely absent on the image edges. Second, the largest RMS values are not located at the same axial locations: for the CVF flow, the largest values of the scalar RMS are located at $2D$, whereas for the VVF, these maxima are distributed much closer to the nozzle, $(0.5D - 1D)$. This observation is to be understood in connection with the instantaneous images. The intense fluctuations are strongly correlated with the presence of the large structure – Kelvin Helmholtz. For the VVF case, while at $x/D = 1$ engulfment only occurs, the mixing exhibits smaller and smaller scales at $x/D = 2$.

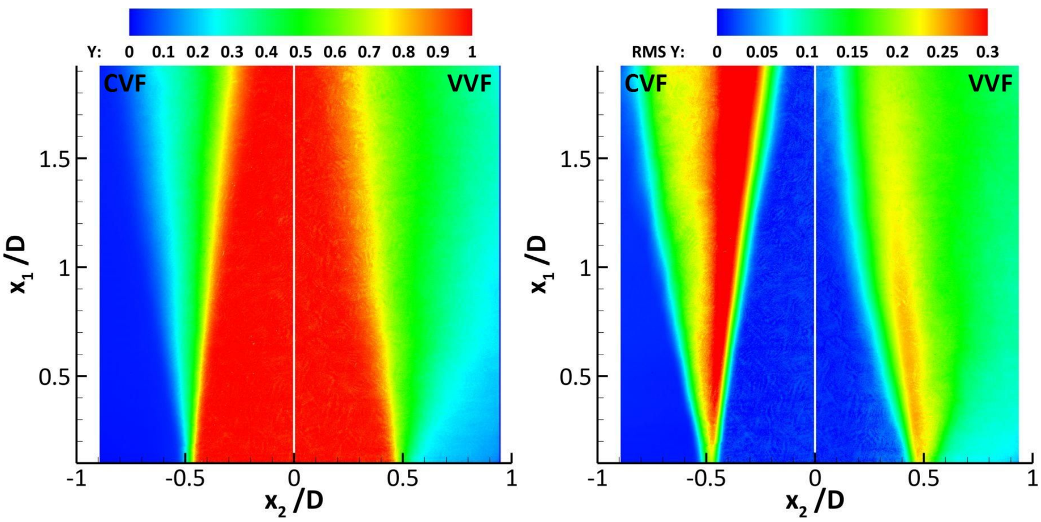

Fig. 7 Planar distributions of the scalar mean (left) and RMS (right) in CVF (N_2/N_2 jet), image left-half-side, and VVF (Propane/N_2 jet), image right-half-side.

As far as the CVF is concerned, only large-scale mixing occurs, thus explaining that larger fluctuations are observed, compared to the VVF case. This observation is strengthened by the study of the velocity field and more particularly of the mean lateral fluctuations (not shown here), whose evolution is similar to that of the scalar. Indeed, at a downstream position of one diameter, the lateral fluctuations are more intense in VVF than in CVF.

Moreover, a stronger decrease of the axial mean velocity in VVF than in CVF is also noticeable, starting in the very early stage of injection, Fig. 8, indicating an increased entrainment of the ambient fluid into the jet fluid and an accelerated trend towards self-similarity. Intense values of the axial velocity fluctuations, Fig. 9, as well as a faster trend towards isotropy (here quantified through the ratio RMS_{u_1}/RMS_{u_2}, Fig. 10, u_1 and u_2 being the axial and radial velocities, respectively) in VVF than in the baseline case (CVF) are observed. These results

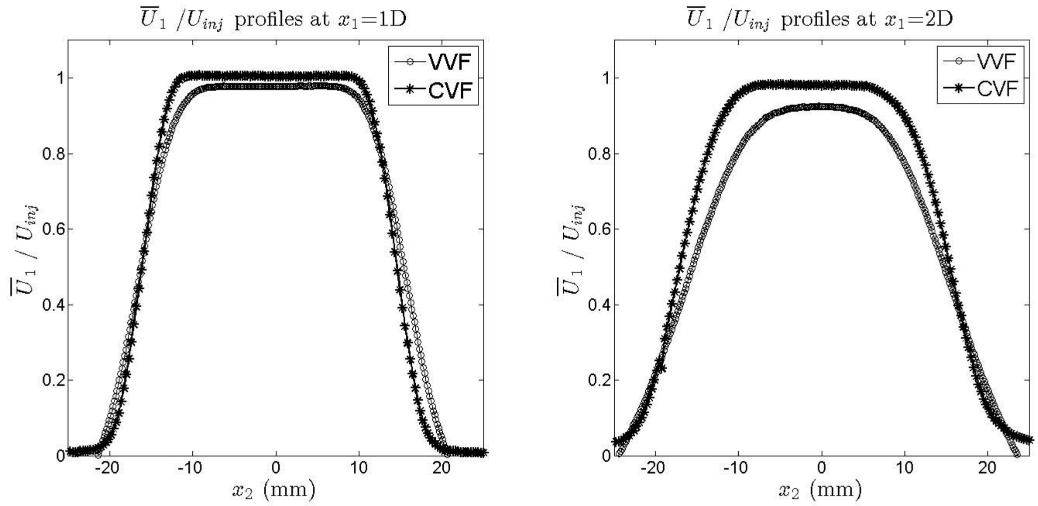

Fig. 8 Mean axial velocity normalized with respect to the injection velocity, for both CVF and VVF, at two axial locations: $x_1 = 1D$ and $x_1 = 2D$.

confirm the trends previously reported by [4], along with the value of 1.2 for the RMS_{u_1}/RMS_{u_2} ratio [13].

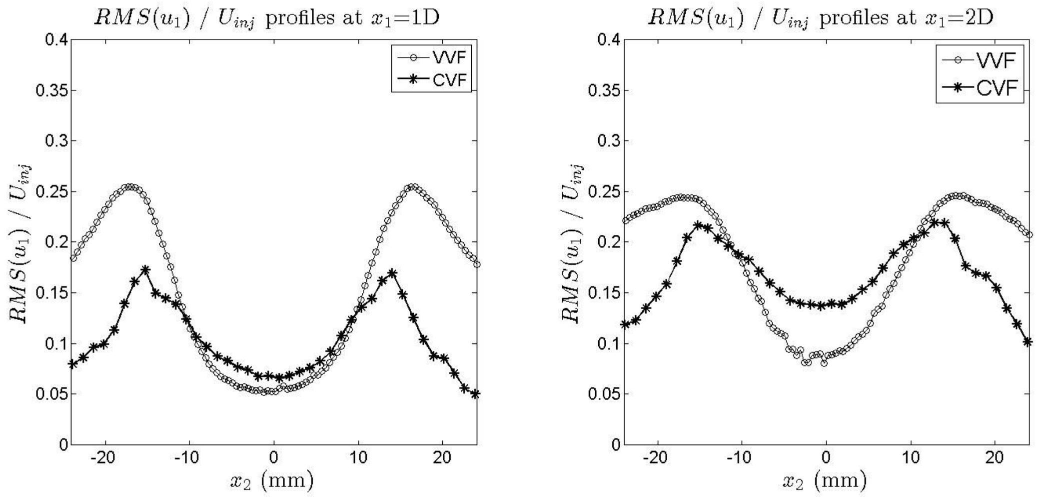

Fig. 9 Radial RMS normalized with respect to the injection velocity, for both CVF and VVF, at two axial locations: $x_1 = 1D$ and $x_1 = 2D$.

The birth of the turbulent fluctuations most likely results from a combination of four factors: *i*) Kelvin Helmholtz instabilities; *ii*) wake instabilities behind the injector lip; *iii*) interface instabilities due to density gradients; *iv*) interface instabilities due to viscosity jumps. Points *i*) and *ii*) are characteristic of jet flows, constant-viscosity or not, thus, they cant be responsible for such different behaviours. As far as the density effects are concerned, the studied configuration is those of a 'heavy jet' (heavy fluid injected in a lighter one). Yet, according to [2], in this situation if the density effects prevailed they would inhibit the mixing and not enhance it as observed here. A phenomenological scenario to explain the mixing enhancement, based on point *iv*), is as follows. Viscous host fluid blobs are brought (via the three types of instabilities) into the jet fluid. These viscous blobs represent obstacles which slow down the initial jet velocity and lead to the production of radial velocity fluctuations behind these obstacles (wake instabilities). The rapid birth of radial velocity fluctuations accelerates the trend towards isotropy and self-similarity.

We conclude this section with the statement that clear experimental evidence has been brought to claim that viscosity stratification has an important influence on turbulence, for viscosity ratios as low as 3.5.

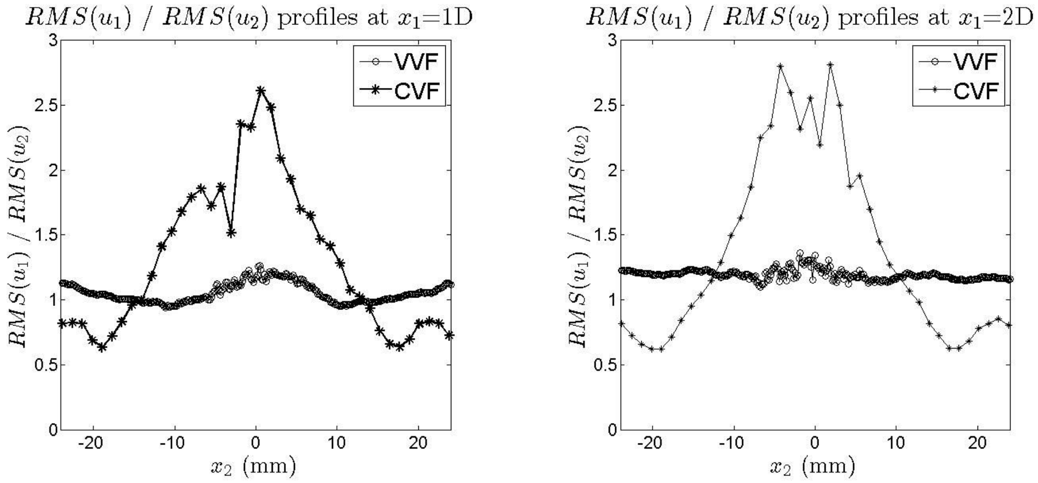

Fig. 10 Ratio RMS_{u_1}/RMS_{u_2} for VVF and CVF, at two axial locations:$x_1 = 1D$ and $x_1 = 2D$.

5 Comparison of VVF and CVF based on the same Reynolds number

In the previous section, we have compared CVF and VVF for the same jet momentum. One could argue that the Reynolds number in the N_2 jet is then 3.5 times lower than propane jet, explaining the observed discrepancies. To refute this argument, we have performed measurements in the CVF case with the same Reynolds number as in the VVF case *i.e* with an injection velocity $U_{inj} = 4.37$ m/s.
Once again, the topology of the two cases is completely different, Fig. 11. If the CVF case is indeed more turbulent than previously (Fig. 6), however it still does not present the large range of scales exhibited by the variable-viscosity flow. The map of the scalar mean, Fig. 12, left, reveals a shift in the virtual origin of the

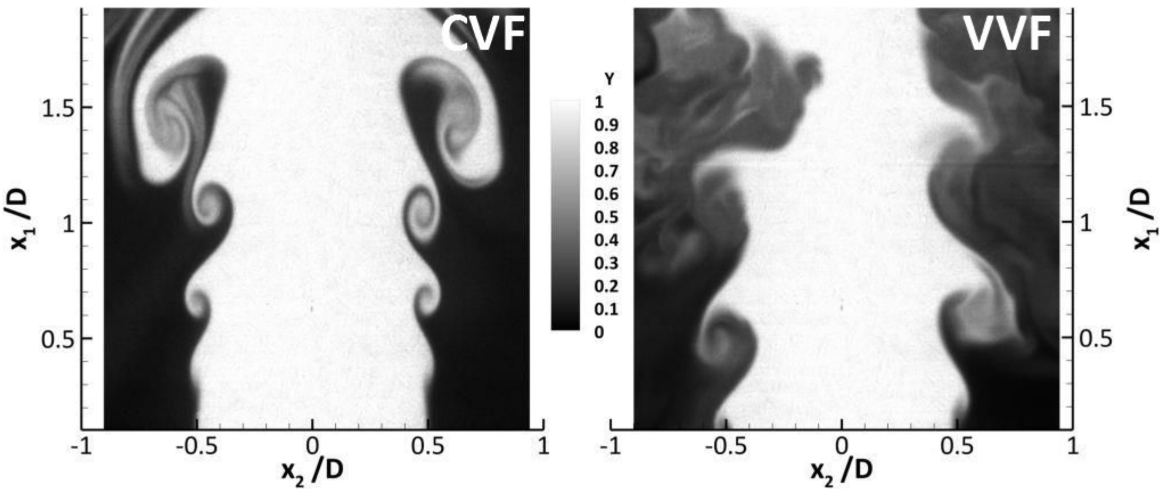

Fig. 11 Instantaneous images of mixing in N_2/N_2 jet (left) and variable-viscosity (Propane/N_2) jet (right).

N_2/N_2 jet compared to the constant-viscosity case detailed in the previous section. As far as the jet angle is concerned, it is smaller in the CVF case than in the VVF case indicating a less advanced mixing.
The maxima of the RMS of the longitudinal fluctuations are once again correlated with the presence of large structures, Fig. 12, right. This is particularly visible when looking at the top of the image (from x_1=1.2 D up to x_1=1.9 D). Indeed, this is the largest zone of intense fluctuations. Confronting with the instantaneous image, Fig. 11, left, it also corresponds to the location of the largest structures. Thus, even if the CVF topology differs slightly from that of the previous section (Sec. 4, same jet momentum), up to this point the observations previously made still hold.
Looking at the dynamic field, at the same axial location, the mean velocity profiles present a more advanced decrease in the variable-viscosity case than in the N_2/N_2 jet, Fig. 13. Similarly, the longitudinal fluctuations

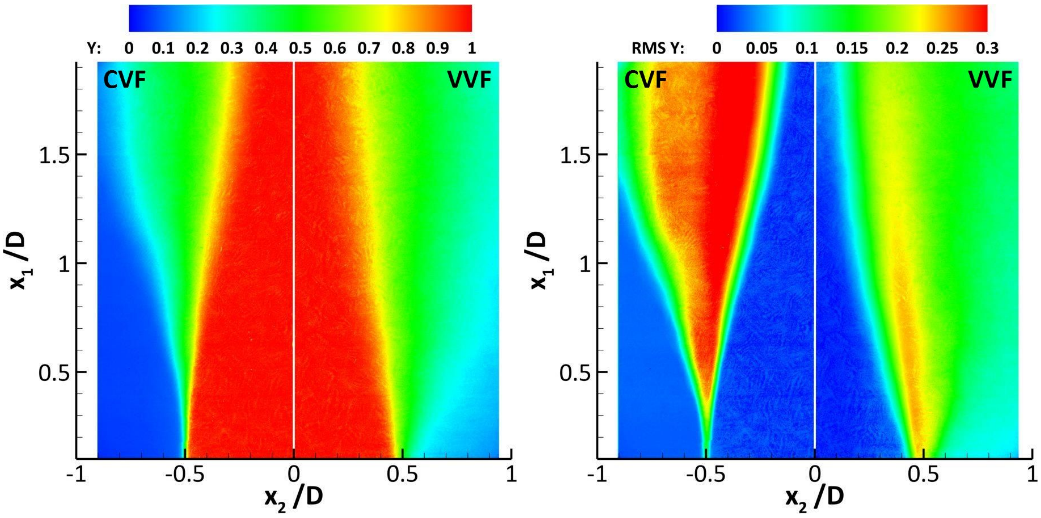

Fig. 12 Planar distributions of the scalar mean (left) and RMS (right) in CVF (N_2/N_2 jet), image left-half-side, and VVF (Propane/N_2 jet), image right-half-side.

are stronger in the VVF case and seem to have started their decrease contrary to those in the CVF which still increase with the axial location, Fig. 14.

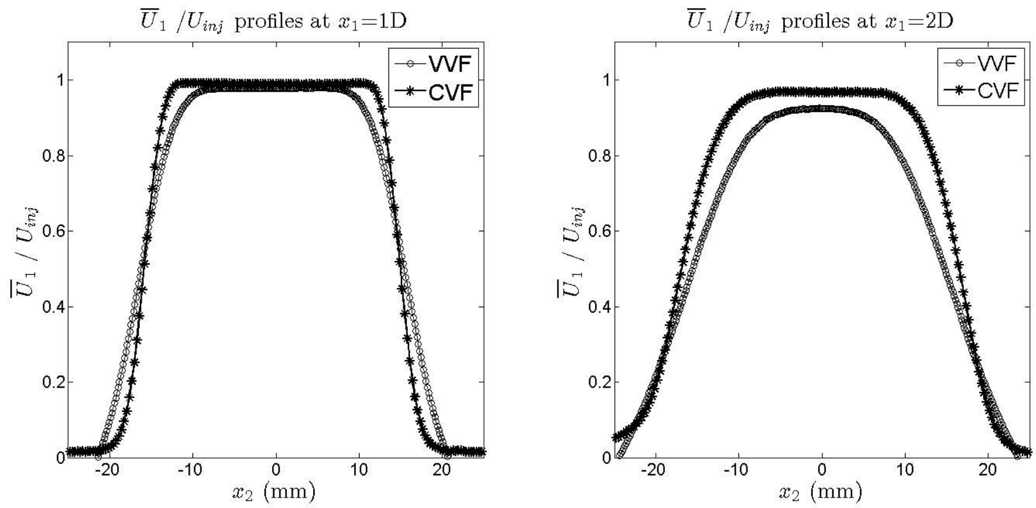

Fig. 13 Mean axial velocity normalized with respect to the injection velocity, for both CVF and VVF, at two axial locations: $x_1 = 1D$ and $x_1 = 2D$.

To conclude, this section illustrates that the discrepancies are still present, even if a little less pronounced, when comparing a VVF and a CVF with the same Reynolds number (*i.e.* different injection velocities).

6 Conclusion

With respect to the classical constant-viscosity jet, the variable-viscosity jet of a fluid issuing into a more viscous ambient, exhibits in the very near field:
– enhanced entrainment
– more important turbulent fluctuations.
We explain these phenomena by stating that if the different 'steps' of the turbulence are the same by nature (birth, growth, decrease and death), their duration is shorter in VVF than in CVF. Moreover, processes like fluctuation production are more intense in flow with variable viscosities. It means that, even when the viscosity gradients disappear (far from the injection where the mixing is achieved), they have already significantly

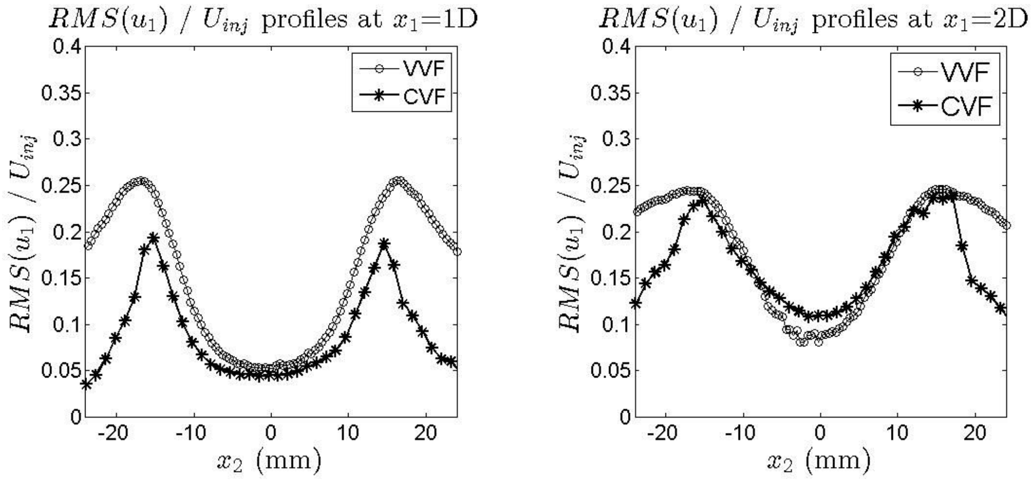

Fig. 14 Radial RMS normalized with respect to the injection velocity, for both CVF and VVF, at two axial locations: $x_1 = 1D$ and $x_1 = 2D$.

modified the flow dynamics. Thus, its final state will be different from a flow which has not be subjected to viscosity effects, even if their initial conditions – Re or jet momentum – are identical. The general message of this contribution is that whereas the viscosity itself indeed acts at the level of smallest scales, flows with viscosity variations at a large scale (such as jets issuing in different environment) are characterised by effects of viscosity variations at any scale, including the largest. A simple visualisation of the scalar dispersion allows us to observe a significant disparity between VVF and CVF behaviours, leading us to state that the viscosity affects the topology and the dynamics of the whole flow at all scales.

Acknowledgements
Financial support from the French National Research Agency, under the project 'MUVAR' is gratefully acknowledged. We thank Dr. G. Godard, A. Vandel and C. Gobin for their helpful assistance in the experimental set up. The authors thank H. Cavalier for its expertise in safety procedures concerning flammable mixtures.

References

[1] Pitts WM (1991) Effects of global density ratio on the centerline mixing behavior of axisymmetric turbulent jets. *Experiments in Fluids*, vol.11, pp 125-134.

[2] Amielh M, Djeridane T, Anselmet F, Fulachier L (1996) Velocity near-field of variable density turbulent jets. *International Journal of Heat and mass transfer*, vol.39, pp.2149-2164.

[3] Campbell IH, Turner JS, (1986) The influence of viscosity on fountains in magma chamber. *Journal of Petrology*, vol.27, pp 1-30.

[4] Talbot B, Danaila L, Renou B (2013) Variable-viscosity mixing in the very near field of a round jet. *Physica Scripta*, vol.T155, pp 014006.

[5] Lee K, Girimaji S, Kerimo J (2008) Validity of Taylor's dissipation-viscosity independence postulate in variable-viscosity turbulent fluid mixtures. *Physical Revue Letter* American Physical Society, vol.101, pp 074501.

[6] Antonia RA, Zhao Q (2001) Effects of initial conditions on a circular jet. *Experiments in Fluids*, vol. 31, pp 319-323.

[7] Bell JH, Mehta RD (1988) Contraction Design For Small Low-Speed Wind Tunnel. *JIAA*, TR-84, pp 1-37.

[8] Lozano A, Yip B, Hanson R (1992) Acetone: a tracer for concentration measurements in gaseous flows by planar laser-induced fluorescence. *Experiments in Fluids*, vol.13(6), pp.369-376.

[9] Schulz C, Sick V (2005) Tracer-LIF diagnostics: quantitative measurement of fuel concentration, temperature and fuel/air ratio in practical combustion systems. *Progress in Energy and Combustion Science*, vol.31, pp 75-121.

[10] Pasquier N, Lecordier B, Trinité M, Cessou A (2007). Investigation of flame propagation through a stratified mixture by simultaneous PIV/LIF measurements. In: Proceedings of the Combustion Institute, vol.31, no 1, p. 1567-1574.

[11] Berlmann I (1971) Handbook of Fluorescence Spectra of Aromatic Molecules. 2nd Edition, Academic Press

[12] Dimotakis PE, Catrakis H and Fourguette D (2001) Flow structure and optical beam propagation in high-Reynolds-number gas-phase shear layers and jets. *Journal of Fluids Mechanics*, vol.433, pp 105-134.

[13] Talbot B, Mazellier N, Renou B, Danaila L and Boukhalfa M (2009) Time-resolved velocity and concentration measurements in variable-viscosity turbulent jet flow. *Experiments in Fluids*, vol.47, pp 769-787.